



1 **Distinct Impacts of El Niño-Southern Oscillation and Indian Ocean Dipole**
2 **on China's Gross Primary Production**

3 Ran Yan^{1,2}, Jun Wang^{1,2*}, Weimin Ju^{1,2*}, Xiuli Xing³, Miao Yu⁴, Meirong Wang⁴, Jingye Tan¹

4 ², Xunmei Wang^{1,2}, Hengmao Wang^{1,2}, Fei Jiang^{1,2}

5 ¹Frontiers Science Center for Critical Earth Material Cycling, International Institute for Earth System Science,
6 Nanjing University, Nanjing, Jiangsu 210023, China

7 ²Jiangsu Provincial Key Laboratory of Geographic Information Science and Technology, Key Laboratory for Land
8 Satellite Remote Sensing Applications of Ministry of Natural Resources, School of Geography and Ocean Science,
9 Nanjing University, Nanjing, Jiangsu 210023, China

10 ³Department of Environmental Science and Engineering, Fudan University, No. 2005, Songhu Road, Yangpu
11 District, Shanghai 200438, China

12 ⁴Joint Center for Data Assimilation Research and Applications/Key Laboratory of Meteorological Disaster,
13 Ministry of Education/Joint International Research Laboratory of Climate and Environment Change (ILCEC)/
14 Collaborative Innovation Center ON Forecast and Evaluation of Meteorological Disasters, Nanjing University of
15 Information Science and Technology, Nanjing 210044, China

16 Corresponding author: Jun Wang (wangjun@nju.edu.cn); Weimin Ju (juweimin@nju.edu.cn)

17



18 **Abstract**

19 Gross primary production (GPP) stands as a crucial component in the terrestrial carbon cycle,
20 greatly affected by large-scale circulation adjustments. This study explores the influence of El
21 Niño-Southern Oscillation (ENSO) and Indian Ocean Dipole (IOD) on China's GPP, utilizing
22 long-term GPP data generated by the Boreal Ecosystem Productivity Simulator (BEPS). Partial
23 correlation coefficients between GPP and ENSO reveal substantial negative associations in
24 most parts of western and northern China during the September-October-November (SON)
25 period of ENSO development. These correlations shift to strongly positive over southern China
26 in December-January-February (DJF), then weaken in March-April-May (MAM) in the
27 following year, eventually turning generally negative over southwestern and northeastern China
28 in June-July-August (JJA). In contrast, the relationship between GPP and IOD basically exhibits
29 opposite seasonal patterns. Composite analysis further confirms these seasonal GPP anomalous
30 patterns. Mechanistically, we ascertain that, in general, these variations are predominantly
31 controlled by soil moisture in SON and JJA, but temperature in DJF and MAM. Quantitatively,
32 China's annual GPP demonstrates modest positive anomalies in La Niña and nIOD years, in
33 contrast to minor negative anomalies in El Niño and pIOD years. This results from
34 counterbalancing effects with significantly greater GPP anomalous magnitudes in DJF and JJA.
35 Additionally, the relative changes in total GPP anomalies at the provincial scale display an east-
36 west pattern in annual variation, while the influence of IOD events on GPP presents an opposing
37 north-south pattern. We believe that this study can significantly contribute to our
38 comprehension of how intricate atmospheric dynamics influence China's GPP on an
39 interannual scale.

40

41 **Key words:** Gross primary production, China, El Niño-Southern Oscillation, Indian Ocean
42 Dipole, BEPS

43

44 **Highlight**

45 (1) Impacts of ENSO and IOD on China's GPP vary with seasons, showing nearly opposite



46 patterns.

47 (2) Soil moisture controls GPP in fall and summer, while temperature plays a key role in
48 winter and spring.

49 (3) Counterbalancing causes modest positive GPP anomalies in La Niña and nIOD,
50 contrasting with minor negative anomalies in El Niño and pIOD.

51

52 **1.Introduction**

53 Vegetation photosynthesis, a pivotal physiological process affecting the terrestrial carbon cycle,
54 predominantly governs variations in the net biome productivity (NBP), surpassing the impact
55 of total ecosystem respiration (Piao et al., 2020; Wang et al., 2022; Wang et al., 2018). Gross
56 primary production (GPP) represents the total amount of carbon dioxide assimilated by plants
57 per unit time through the photosynthetic processes, acting as a crucial carbon flux in mitigating
58 anthropogenic CO₂ emissions (Gough, 2012; Houghton, 2007). However, despite evident long-
59 term increasing trends in GPP, primarily attributed to CO₂ fertilization (Ryu et al., 2019;
60 Schimel et al., 2015; Yang et al., 2022), it also shows regional and global interannual variations.
61 These variations are largely linked to climate fluctuations driven by ocean-atmosphere
62 interactions and the teleconnections (Wang et al., 2021b; Ying et al., 2022). To date, the impact
63 of such teleconnections on China's GPP remains insufficiently documented.

64

65 The El Niño-Southern Oscillation (ENSO) exerts a significant influence on the global terrestrial
66 carbon cycle, which is the dominant mode of inter-annual climate variability (Bauch, 2020;
67 Kim et al., 2017; Wang et al., 2016; Wang et al., 2018; Zeng et al., 2005). Within this context,
68 GPP typically assumes a leading role in shaping the response of terrestrial carbon sinks to
69 ENSO events (Ahlstrom et al., 2015; Wang et al., 2018; Zhang et al., 2018). Global patterns
70 reveal a negative GPP anomaly of approximately $-1.08 \text{ Pg C yr}^{-1}$ during El Niño years,
71 contrasting a positive GPP anomaly of about $1.63 \text{ Pg C yr}^{-1}$ in La Niña years (Zhang et al.,
72 2019). However, the impact of ENSO on GPP exhibits significant regional differences. At



73 present, while existing researches have predominantly focused on the response of tropical GPP
74 to ENSO, studies specific to China are relatively limited. Liu et al. (2014) highlighted the effects
75 of ENSO on crop growth in the North China, and Li et al. (2021) demonstrated that the response
76 of GPP to El Niño varies with the phase of the Pacific Decadal Oscillation (PDO) in the eastern
77 China.

78
79 ENSO is not the sole global climatic oscillation, influencing the terrestrial carbon cycle.
80 Another significant player is the Indian Ocean Dipole (IOD), a tropical coupled ocean-
81 atmosphere mode (Saji et al., 1999), which also affects the terrestrial carbon cycling by
82 modulating the climate circulations (Wang et al., 2022; Wang et al., 2020; Wang et al., 2021b;
83 Yan et al., 2023). Research indicates that IOD events can influence precipitation in China, with
84 effects lasting from the year of the event through the subsequent summer (Zhang et al., 2022a).
85 Zhang et al. (2022b) also proved that extreme pIOD events in 2019 affected the precipitation in
86 summer 2020 in Eastern China, and proposed that the summer precipitation in the following
87 year was mainly affected by IOD in northern China, while by ENSO in the Yangtze River Basin.
88 Additionally, a prior study explored the influence of the extreme positive IOD (pIOD) event in
89 2019 on GPP anomalies across the Indian Ocean rim countries. It suggested a conspicuous
90 negative GPP anomaly occurred in eastern China during the September-October-November
91 (SON) (Wang et al., 2021b).

92
93 The primary objective of this study was to comprehensively assess the impact of ENSO and
94 IOD events on GPP in China. To this end, we initially employed partial correlation analysis to
95 elucidate the relationship between GPP and climate anomalies, specifically soil moisture and
96 temperature, induced by ENSO and IOD events across various seasons. The analysis utilized
97 historical long-term GPP data spanning from 1981 to 2021, simulated by the Boreal Ecosystem
98 Productivity Simulator (BEPS) model. The aim was to get a preliminary understanding of the
99 influence exerted by ENSO and IOD. Furthermore, composite analysis was adopted to illustrate
100 the actual responses during distinct events, including individual ENSO and IOD occurrences.



101 The ensuing discussion will delve into the analysis results on national, regional, and provincial
102 scales.

103

104 **2.Datasets and methods**

105 **2.1 Datasets used**

106 The sea surface temperature (SST) dataset are derived from the Monthly NOAA's Extended
107 Reconstructed Sea Surface Temperature version 5 (ERSSTv5) (Muñoz, 2019). It is generated
108 on a $2^{\circ} \times 2^{\circ}$ grid, using statistical methods to enhance spatial completeness. Commencing from
109 January 1854 to the present, the monthly SST data includes anomalies computed with respect
110 to a 1971-2000 monthly climatology.

111

112 Meteorological data were adopted from ERA5-Land monthly averaged data with $0.1^{\circ} \times 0.1^{\circ}$
113 grids, including 2m surface air temperature (TAS), and volumetric soil moisture (SM) during
114 the period from 1981 to 2021. ERA5-Land was created by replaying the land component of the
115 ECMWF ERA5 climate reanalysis at a higher resolution compared to ERA5. Reanalysis
116 combines model data with global observations into a consistent dataset based on the laws of
117 physics. The original soil moisture data was divided into four layers based on different surface
118 depths. These layers were depth-weighted and then aggregated into the average soil moisture
119 to a depth of 289cm ($\text{m}^3 \text{m}^{-3}$).

120

121 GPP spanning from 1981 to 2021 was simulated by the BEPS model, featuring a horizontal
122 resolution of $0.0727^{\circ} \times 0.0727^{\circ}$. The BEPS model, originally developed for Canadian boreal
123 ecosystems, has been re-constructed for GPP simulations on the global scale (Chen et al., 1999;
124 Chen et al., 2012). BEPS is a process-based model driven by satellite-observed leaf area index
125 (LAI), meteorological data, land cover types, soil texture, and CO_2 concentration to simulate
126 the daily carbon flux of terrestrial ecosystems (Chen et al., 2019; Liu et al., 1997). The input



127 data used to drive GPP in this study include ERA5 meteorological data (Hersbach et al., 2023),
128 GLOBMAP LAI product (Liu et al., 2012), Land Cover Classification System (LCCS)
129 generated by the Food and Agriculture Organization (FAO) of the United Nations (Friedl and
130 Sulla-Menashe, 2019), Harmonized World Soil Database v1.2 from FAO (Fischer et al., 2008),
131 and CO₂ concentration based on the Global Monitoring Laboratory from NASA (Lan et al.).
132 Notably, BEPS distinguishes itself from other models through the organic combination of
133 remote sensing data and mechanistic modelling. It produces simulation datasets for GPP, Net
134 primary productivity (NPP) and evapotranspiration (ET). Key features of BEPS include the
135 incorporation of sunlit-shaded leaf stratification strategy (Norman, 1982). The model calculates
136 canopy-level photosynthesis by summing the GPP of sunlit and shaded leaves (Chen et al.,
137 1999).

$$138 \quad GPP = A_{sun}LAI_{sun} + A_{shade}LAI_{shade} \quad (1)$$

$$139 \quad LAI_{sun} = 2 \cos \theta \left[1 - \exp \left(- \frac{0.5\Omega LAI}{\cos \theta} \right) \right] \quad (2)$$

$$140 \quad LAI_{shade} = 1 - LAI_{sun} \quad (3)$$

141 where A_{sun} and A_{shade} represent the amount of photosynthesis at per sunlit and shaded leaf,
142 respectively; LAI_{sun} and LAI_{shade} represent the canopy-level sunlit and shaded LAI,
143 respectively; Ω is the foliage clumping index indicating the influence of foliage clustering on
144 radiation transmission, and θ is the solar zenith angle.

145 The accuracy of carbon flux products simulated by BEPS has been validated in previous studies
146 (Chen et al., 2019; He et al., 2021). We also used the measured site data from ChinaFlux
147 (<http://chinaflux.org/>) and National Tibetan Plateau Third Pole Environment (Li et al., 2013)
148 (Table S1) to assess the performance of BEPS simulated GPP (Fig. S1). Our analysis reveals a
149 high consistency between simulated and observed GPP, with an average R² of 0.77 ($p < 0.05$)
150 and an average root mean square error (RMSE) of 1.70 gC m⁻² day⁻¹. In addition, the global
151 terrestrial GPP from FluxSat product Version 2.2 (Joiner et al., 2018) was also used to assess
152 the reliability of BEPS GPP. FluxSat GPP is obtained by using light-use efficiency (LUE)
153 framework based on Moderate-resolution Imaging Spectroradiometer (MODIS) satellite data,
154 eliminating the dependency on other meteorological input data. The comparison between BEPS



155 GPP and FluxSat GPP data revealed a robust agreement, with a correlation coefficient (r) of
156 0.63 ($p < 0.05$) and a RMSE of 1.1 Pg C yr^{-1} (Fig. S2). These consistencies underscore the
157 reliability of the BEPS GPP data in capturing terrestrial carbon flux dynamics.

158 **2.2 Anomaly calculation**

159 To calculate anomalies, we initially eliminated the long-term climatology to get rid of the
160 seasonal cycle. Subsequently, we subtracted the 7-year running average for each grid to
161 eliminate the decadal oscillation and long-term trends for all the variables. Further, refinement
162 involved smoothing the derived GPP and climate anomalies using a 3-month running average
163 to remove the intra-seasonal variability. For consistency, the BEPS simulated GPP data was
164 resampled to $0.1^\circ \times 0.1^\circ$. To align with this, non-vegetated areas in the climate data were
165 masked according to the resampled BEPS GPP, uniformity in spatial representation.

166 **2.3 Definition of climate events**

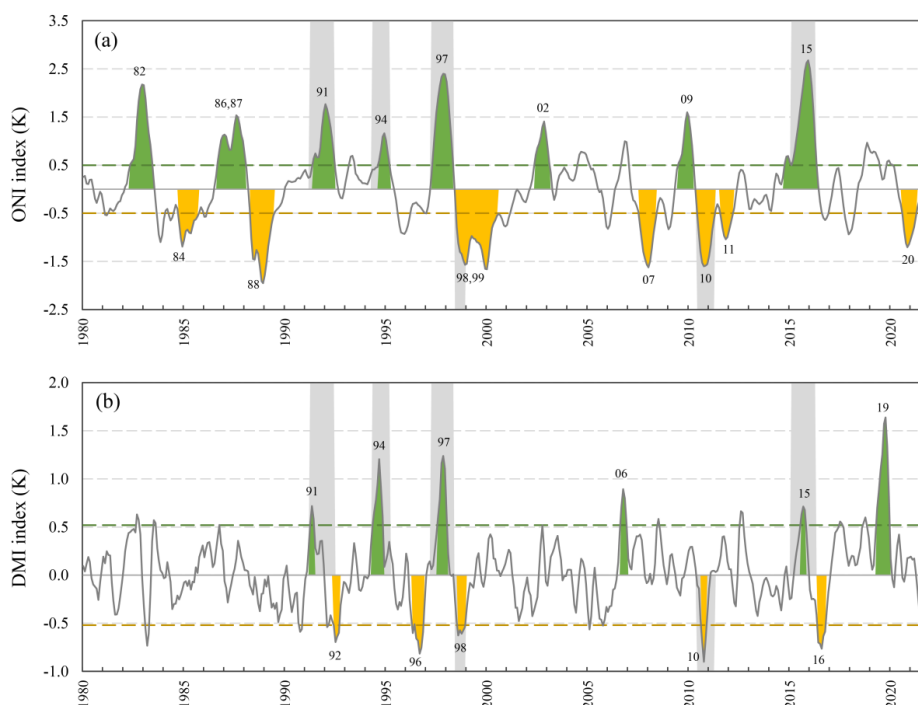
167 The Oceanic Niño Index (ONI) is used to define ENSO events (Fig. 1a), which represents the
168 3-month running mean SST anomaly in the Niño 3.4 region (5°N - 5°S , 120° - 170°W). The
169 positive phase of an ENSO event (El Niño) is characterized by the ONI exceeding $+0.5\text{K}$ for
170 five consecutive overlapping 3-month periods. Conversely, the negative phase of an ENSO
171 event (La Niña) occurs when the ONI is below -0.5K for five consecutive overlapping 3-month
172 periods. The severity of the event can be further categorized into weak (0.5 - 0.99), moderate
173 (1.00 - 1.49), strong (1.50 - 1.99) and extremely strong (≥ 2.00) based on the absolute value of
174 the ONI. To qualify for a specific rating, an event should meet or exceed a threshold for at least
175 three consecutive overlapping three-month periods.

176

177 Moreover, the Dipole Mode Index (DMI) is employed to identify IOD events (Saji et al., 1999).
178 The DMI is calculated from SST differences between the Western Equatorial Indian Ocean
179 (10°S - 10°N , 50° - 70°E) and the South-eastern Equatorial Indian Ocean (10°S - 0°N , 90° - 110°E)
180 (Fig.1b). Given that the short duration of IOD events with a tendency to peak during the SON,



181 the standard deviation of SON DMI (0.52K from 1981 to 2021) is used as the criterion for
182 identifying IOD events. A positive phase IOD (pIOD) event is defined when the absolute value
183 of DMI is greater than or equal to one standard deviation (0.52 K) for three consecutive 3-
184 month periods. Additionally, a strong pIOD event is identified if the DMI value exceeds two
185 standard deviations (1.04 K).



186
187 Fig.1 Time series of the Oceanic Niño Index (ONI) (a) and the Dipole Mode Index (DMI) (b) from 1980
188 to 2022. The positive phase events (El Niño and positive Indian Ocean Dipole (pIOD)) are filled in
189 green and the negative phase events (La Niña and negative IOD (nIOD)) are filled in yellow, and the
190 events are also labeled with a two-digit year. The green and yellow dashed lines represent the positive
191 and negative thresholds for El Niño-Southern Oscillation (ENSO) and IOD, respectively. The gray
192 background indicates years with the simultaneous ENSO and IOD events.

193 2.4 Partial correlation analysis

194 To comprehensively assess the impacts of ENSO and IOD on GPP, while accounting for the



195 influence of other events, partial correlation analysis (pcor) was employed, following the
 196 previous studies (Saji and Yamagata, 2003; Wang et al., 2021b). The definition of *pcor* for *x*
 197 and *y*, controlling for *z*, is given by:

$$198 \quad pcor_{yx.z} = \frac{r_{yx} - r_{yz}r_{xz}}{\sqrt{1-r_{yz}^2}\sqrt{1-r_{xz}^2}} \quad (4)$$

199 where r_{yx} is the correlation of the dependent variable *y* and the explanatory variable *x* (e.g.,
 200 DMI), and the same is for r_{yz} and r_{yx} . The two-tailed Student's *t*-test was used to calculate
 201 the statistical significance of each pixel result:

$$202 \quad t = pcor_{yx.z} \sqrt{\frac{n-2-k}{1-pcor_{yx.z}^2}} \quad (5)$$

203 where *n* and *k* are the number of samples and conditioned variables, respectively.

204

205 2.5 Composite analysis

206 When enumerating the years of ENSO and IOD events, we retained all the years of IOD events
 207 and ENSO events of above the moderate intensity. Individual events and compound events were
 208 categorized and summarized in Table 1. In this study, a compound event refers to the
 209 simultaneous occurrence of ENSO and IOD, primarily El Niño & pIOD and La Niña & negative
 210 IOD (nIOD). IOD typically peaked in the September-October-November (SON, yr0), while
 211 ENSO peaked in the December(yr0)-January(yr1)-February(yr1) (DJF), and the influence of
 212 the two events could extend until the summer of the following year. Therefore, we selected four
 213 seasons from SON to June-July-August (JJA) in the following year for composite analysis in
 214 this study. In addition, the year 1991 was excluded due to the strong eruption of Mount Pinatubo,
 215 which had a large impact on the global carbon cycle (Mercado et al., 2009).

216

217 **Table 1.** Occurrences of ENSO and IOD events from 1981 to 2021.

Events	Years
El Niño	1982, 1986, 1987, 2002, 2009
La Niña	1984, 1988, 1999, 2007, 2011, 2020



pIOD	2019
nIOD	1992, 1996, 2016
El Niño & pIOD	1994,1997, 2015
El Niño & nIOD	-
La Niña & pIOD	-
La Niña & nIOD	1998, 2010

<https://doi.org/10.5194/egusphere-2024-1250>

Preprint. Discussion started: 10 June 2024

© Author(s) 2024. CC BY 4.0 License.



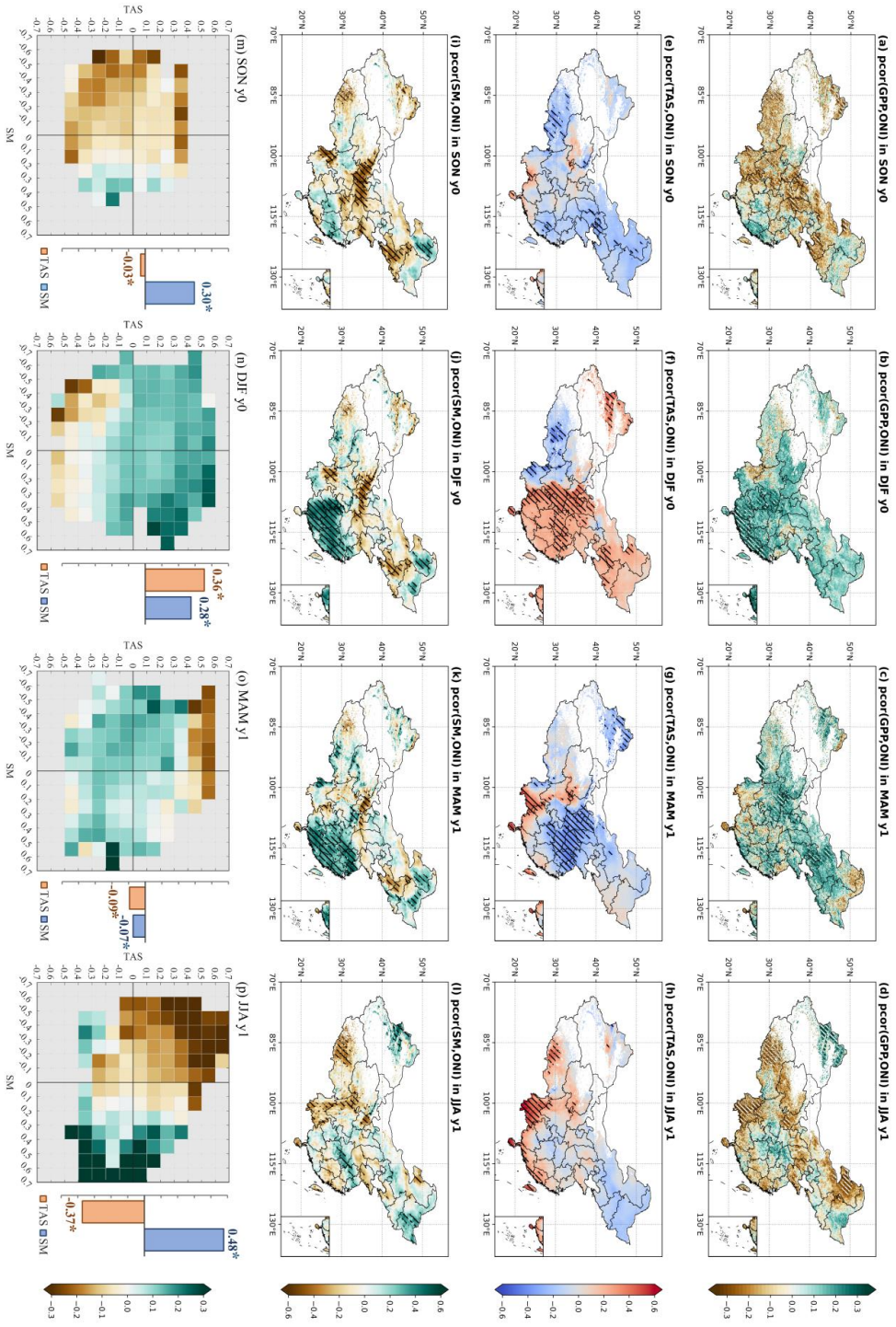
219 **3.Results**

220 **3.1 Historical relationship between GPP and ENSO**



221
 222
 223
 224
 225

Fig. 2 Spatial patterns of partial correlation coefficients (ρ_{cor}) between ONI and gross primary productivity (GPP) (a-d), surface air temperature (TAS) (e-h), soil moisture (SM) (i-l) in different seasons, controlling for the effect of DMI. Hatched areas represent significance at $p \leq 0.05$ based on the two-tailed Student's t -test. (m-p) Heatmaps represent the relationships of the ρ_{cor} patterns among GPP, TAS, and SM, and bar charts illustrate the pattern correlations of these ρ_{cor} values between GPP and TAS and SM on the national scale for each season. Notably, asterisks (*) in the bar charts denote significance at $p < 0.05$.



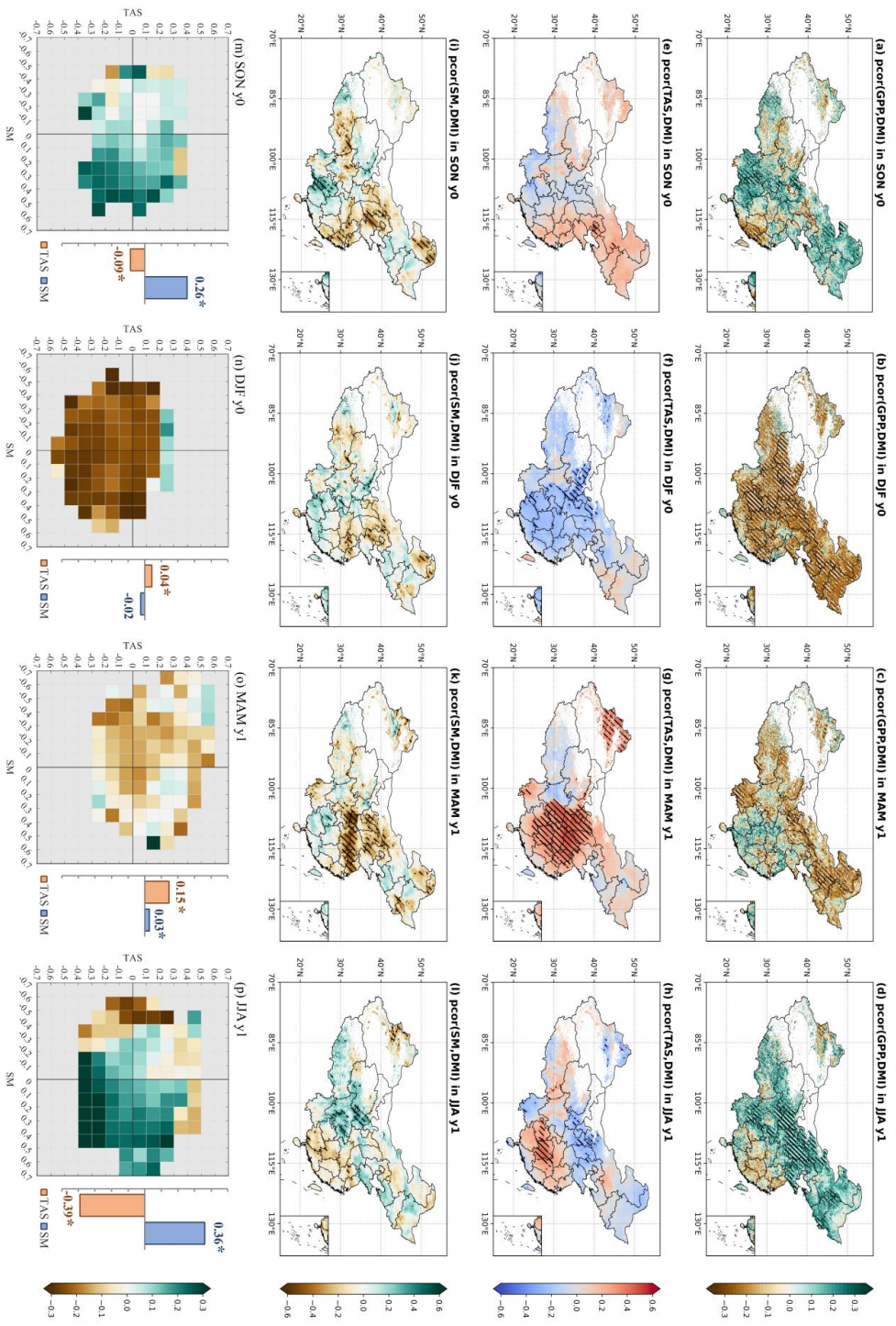


Fig. 3 Same as Fig. 2, but for DMI, controlling the effect of ONI.

226
 227
 228



229 We analyzed the *pcor* patterns between GPP, climate anomalies, and events using long time
230 series data (Figs. 2 and 3). Following this, we calculated pattern correlation coefficients
231 between the GPP and climate *pcor* patterns (including all the pixels over China), aiming to
232 investigate the varying impacts of TAS and SM on photosynthesis across different seasons
233 (Figs. 2m-p, and 3m-p).

234

235 Figure 2 reveals notable seasonal variations in the *pcor* patterns between GPP, related climate
236 anomalies, and ONI index in December-January-February (DJF) when ENSO peaked,
237 controlling the effect of DMI in September-October-November (SON) when IOD peaked.
238 During SON, significant negative *pcor* between GPP and ONI is observed in regions including
239 the Tibetan Plateau, Southwestern China, Loess Plateau, and Liaoning province (Fig. 2a).
240 Clearly, this pattern aligns closely with the *pcor* pattern between soil moisture and ONI (Figs.
241 2a and i). The pattern correlation analysis between GPP and both TAS and SM underscores the
242 dominance of SM in influencing GPP anomalies, indicated by a correlation coefficient of 0.30
243 ($p < 0.05$). This finding suggests that the soil moisture deficit induced by El Niño largely
244 inhibits vegetation photosynthesis during this season (Fig. 2m).

245

246 Along with the peak of ENSO events in DJF, the *pcor* pattern between GPP and ONI exhibits
247 a distinct shift from the pattern in SON. Notably, DJF showcases significant positive *pcor*
248 values over large areas in southern China and weak positive *pcor* in the North and Northeastern
249 China (Fig. 2b). During this period, temperature emerges as a more influential factor in driving
250 GPP changes, reflected in a nation-wide pattern correlation coefficient of 0.36 ($p < 0.05$) (Fig.
251 2n). Specifically, higher winter temperatures during El Niño, coupled with sufficient soil
252 moisture, contribute to a substantial enhancement in GPP across Southern China. In contrast,
253 the impact is weaker in the North and Northeast China due to the vegetation being in the non-
254 growing season, and localized soil water deficits (Figs. 2b, f, and j). In addition, GPP
255 experiences inhibition in some areas of southwestern China due to low temperatures and soil
256 drought.



257

258 Subsequently, the positive *pcor* of GPP decreases, or even turns into weak negative values from
259 DJF to March-April-May (MAM) in southern China. These changes are primarily attributed to
260 shifts of temperature, with a pattern correlation coefficient of -0.09 ($p < 0.05$) (Figs. 2c, g, and
261 o). Conversely, the positive *pcor* of GPP continues to increase in northern Sichuan, aligning
262 with the positive *pcor* of temperature (Figs. 2c and g), and in northern Hebei and parts of
263 neighboring Inner Mongolia, corresponding to the weak positive *pcor* of soil moisture (Figs.
264 2c and k).

265

266 Moving into JJA, the *pcor* of GPP exhibits widespread negative values again (Fig. 2d). In
267 general, during El Niño, increased soil moisture and lower temperatures greatly contribute to
268 enhanced GPP, while drier soil moisture and higher temperatures inhibit the increase in GPP
269 (Fig. 2p). Regionally, higher temperatures and lower soil moisture both contribute to the
270 negative GPP anomalies over southwestern China. However, lower soil moisture
271 predominantly curtails GPP over the Tibetan Plateau, the Yellow River basin, and northeastern
272 Inner Mongolia. Overall, the correlation coefficients between GPP and TAS and SM in summer
273 are comparable, with soil moisture exhibiting a slightly higher effect, represented by a
274 correlation coefficient of 0.48 ($p < 0.05$), compared to a correlation coefficient of -0.37 ($p <$
275 0.05) for temperature.

276

277 3.2 Historical relationship between GPP and IOD

278 In comparison, the *pcor* patterns between GPP and DMI in SON, controlling for the effect of
279 ONI in DJF, exhibit nearly opposite patterns to those between GPP and ONI (Figs. 2 and 3). In
280 detail, GPP demonstrates significant positive *pcor* values with DMI in southwestern China and
281 eastern Inner Mongolia, but displays significant negative *pcor* with DMI in southeastern China
282 during SON (Fig. 3a). In terms of climate drivers, during the pIOD events, for instance, wetter
283 soil and lower temperatures both benefit the significant enhancement in GPP in southwestern



284 China, while higher temperatures largely contribute to the enhancement in GPP over eastern
285 Inner Mongolia. Conversely, GPP is largely inhibited by the dry conditions in southeastern
286 China (Figs. 3e and i). Overall, soil moisture dominates the GPP anomaly in China, with a
287 correlation coefficient of 0.26 ($p < 0.05$) (Fig. 3m).

288

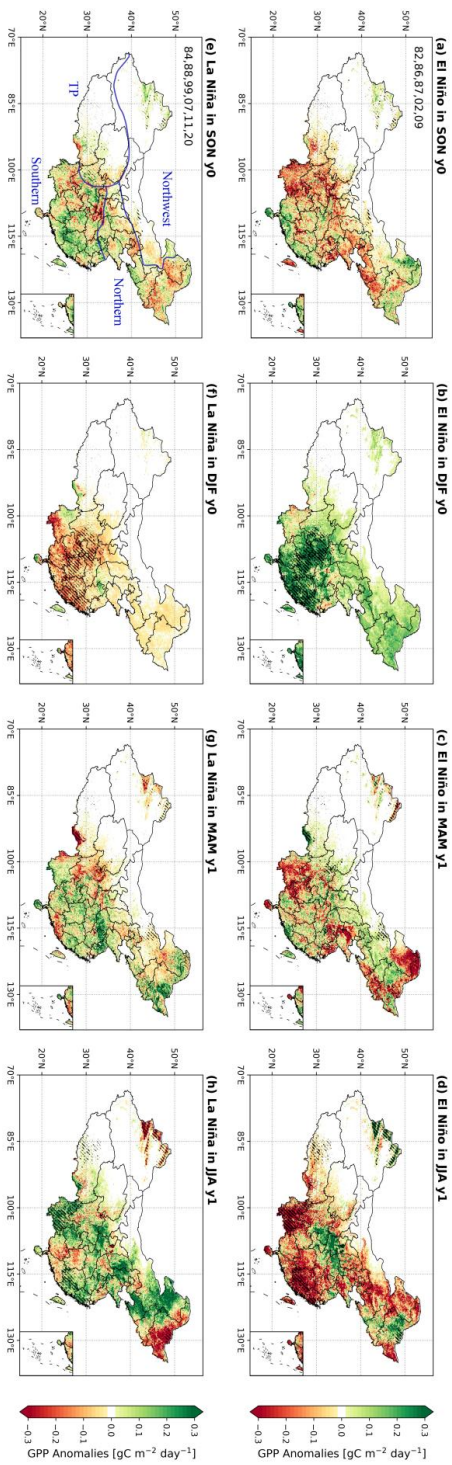
289 In DJF, GPP exhibits widespread significant negative *pcor* with DMI (Fig. 3b), primarily due
290 to the widespread negative *pcor* of temperature, characterized by a correlation coefficient of
291 0.04 ($p < 0.05$) (Figs. 3f and n). Moving into MAM, the significant negative *pcor* between GPP
292 and DMI carried on from those in DJF, but shifts to weak positive *pcor* in southeastern China,
293 driven by the significant positive *pcor* of temperature (Figs. 3c and g). However, the significant
294 negative *pcor* of soil moisture in the Jianghuai Basin and North China still negates the positive
295 effect of temperature (Fig. 3k). During this period, temperature remains the dominant factor,
296 with a nation-wide pattern correlation coefficient of 0.15 ($p < 0.05$) with GPP (Fig. 3o).

297

298 In JJA, the situation undergoes a change, showing the significant positive *pcor* of GPP over
299 southwestern, north and northeast China, and weak negative *pcor* over southeastern China (Fig.
300 3d). In other words, lower temperatures and gradually wetter soil are conducive to the increase
301 in vegetation photosynthesis, but heat and dry conditions cause the weak inhibition of
302 photosynthesis in southeastern China during the pIOD (Figs. 3p). However, unlike the ENSO
303 event, the role of temperature is slightly higher than that of SM in the IOD event, and the
304 correlations between GPP and TAS and SM are -0.39 and 0.36 ($p < 0.05$), respectively.

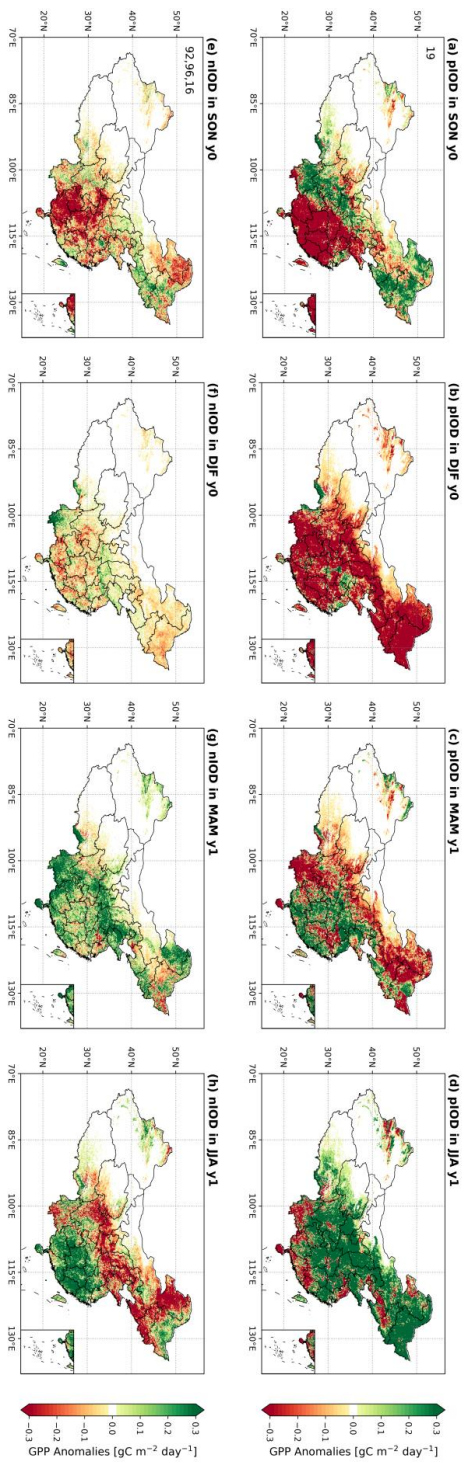
305

306 **3.3 GPP anomalies caused by specific ENSO and IOD events**



307
 308 Fig. 4. Spatial distributions of seasonal composite GPP anomalies for ENSO events, (a-d) for El Niño, and (e-h) for La Niña. The black slashes indicate areas
 309 where El Niño events differ significantly from La Niña events ($p \leq 0.05$) based on the Student's two-sample *t*-test. The two-digit year in first column denote the
 310 years used for composite analysis. Additionally, China is divided into four regions: Northwest China, Tibetan Plateau, Northern China, and Southern China, as
 311 shown in (e), which is used in the following context.
 312





313
 314 Fig. 5. Similar to Fig. 4, but for spatial distributions of seasonal composite GPP anomalies for IOD events, (a-d) for pIOD, and (e-h) for nIOD. We did not
 315 conduct the significance test here owing to the limited samples.
 316



317 While we have elucidated the historical relationship between GPP and ENSO and IOD events
318 through partial correlation coefficients and discussed the underlying climate drivers, we here
319 specifically selected actual events to conduct a composite analysis. This approach aims to
320 further comprehensive understanding of the effects of ENSO and IOD events on GPP variations
321 in China.

322

323 **3.3.1 ENSO-induced GPP anomalous patterns**

324 The impacts of El Niño and La Niña events exhibit opposite influences on GPP with obvious
325 seasonal variations (Fig. 4). Specifically, during SON, GPP anomalies are relatively weak,
326 indicating some suppressions over southwestern China and north China during El Niño events,
327 primarily attributed to dry conditions there (Figs. 4a and S4a). As ENSO peaks in DJF, GPP is
328 significantly strengthened during El Niño events and suppressed during La Niña events,
329 especially over southern China (Figs. 4b and f), aligning well with the patterns of *pcor* between
330 GPP and ONI, controlling the effect of DMI (Fig. 2b). Concurrently, the widespread higher
331 temperatures and wetter soil moisture both contribute to enhanced GPP over southern China
332 during El Niño events (Figs. S3b and S4b), while colder temperatures and drier soil moisture
333 lead to GPP suppression there during La Niña (Figs. 2f and 3f). It is worth mentioning that GPP
334 shows insignificant changes over north China in DJF although soil water deficits are still severe
335 (Fig. S4b). This is mainly because of the non-growing season for vegetation. In MAM as ENSO
336 weakens and vegetation starts to grow in the extratropics, the enhanced GPP over southern
337 China in DJF during El Niño events diminishes, even transitioning into a notable GPP reduction
338 over southwestern China, north China, and northeastern China (Fig. 4c). This transition is
339 conspired by phenological and climate changes including colder temperatures and prolonged
340 dry conditions (Figs. S3c and S4c). The GPP pattern exhibits the opposite transition in La Niña
341 (Fig. 4g). Moving to JJA, dry and hot conditions (Fig. S3d and S4d) lead to significant negative
342 GPP anomalies in southeastern and southwestern China in El Niño (Fig. 4d), whereas cool and
343 wet conditions result in positive GPP anomalies in La Niña events (Fig. 4h). Overall, GPP



344 anomalies induced by ENSO events in DJF and JJA are more pronounced than those in SON
345 and MAM, corresponding to the life cycle of event and vegetation growth periods, respectively.
346 Crucially, they demonstrate distinct GPP patterns, with significant enhancements in DJF and
347 reductions in JJA during El Niño events and reverse during La Niña events, aligning well with
348 the *pcor* pattern between GPP and ONI, controlling for the effect of DMI (Fig. 4). In addition,
349 the effect of ENSO on vegetation in southern China appears more substantial.

350

351 **3.3.2 IOD-induced GPP anomalous patterns**

352 During the period from 1981 to 2021, we only find one independent but extreme pIOD event
353 occurred in 2019 according to our criterion (Table 1). This extreme pIOD event extended from
354 June to December, a longer duration compared to other IOD events. Different from ENSO,
355 IOD basically peaks in SON. GPP anomalies induced by this extreme event align closely with
356 the long-term *pcor* patterns between GPP and DMI, controlling for the effect of ONI (Fig. 3).
357 Specifically, significant reductions in GPP occur in southeastern China in SON (Fig. 5a),
358 predominantly due to heat stress and severe drought conditions (Figs. S5a and S6a), consistent
359 with the findings revealed by Wang et al. (2021b). In DJF, the seasonal legacy of vegetation
360 state (Yan et al., 2023) and prolonged droughts lead to the widespread GPP reductions (Figs.
361 5b and S6b), outweighing the potential positive effect of higher temperatures (Fig. S5b). Of
362 course, the decline of GPP in southwestern China appears linked to lower temperatures (Figs.
363 5b and S5b). During MAM, the mitigation of soil moisture deficit and favorable higher
364 temperatures in southern China facilitate a shift in GPP from decline to increase (Fig. 5c). In
365 the north, persistent drought conditions notwithstanding (Fig. S6c), higher temperatures and
366 the onset of the growing season contribute to the enhanced GPP (Fig. 5c). In JJA, increased
367 precipitation over the Yangtze and Yellow River basins (Zhang et al., 2022) alleviates the soil
368 moisture deficits (Fig. S6d). Coupled with the relatively lower temperatures, this leads to
369 widespread GPP increases. Conversely, GPP suppressions in provinces south of 25°N and
370 around the Bohai Sea are attributed to higher temperatures and soil water deficits (Figs. 5d,



371 S5d, and S6d).

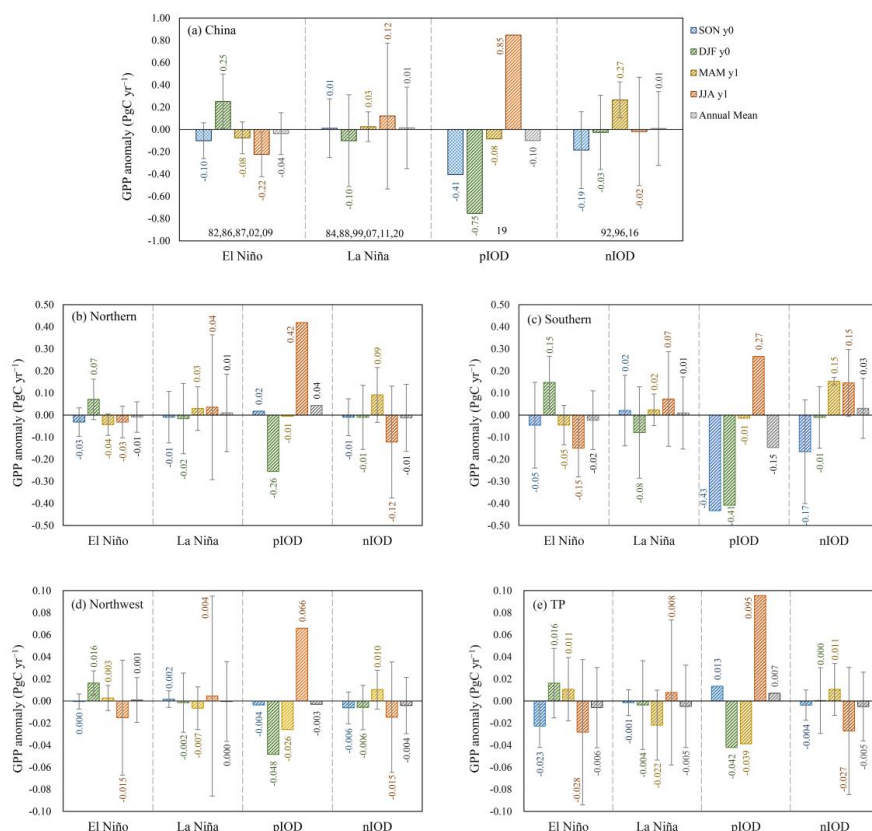
372

373 In contrast to the intense 2019 pIOD event, our composite analysis incorporates three weak
374 nIOD events, resulting in comparatively milder anomalies. In SON, different from pIOD event,
375 negative GPP anomalies in nIOD mainly appear in the provinces of Guizhou, Hunan, and
376 Guangxi (Fig. 5e), associated well with concurrent dry conditions (Fig. S6e). In DJF, although
377 the spatial pattern of soil moisture remains largely consistent with SON (Fig. S6f), a shift from
378 negative to positive temperature anomalies mitigates the evident GPP reductions (Fig. 5f). The
379 ongoing soil wetting and the onset of the growing season in northern hemisphere in MAM
380 result in the increased GPP over the Yellow River Basin and southwestern China (Figs. 5g, S5g,
381 and S6g). Subsequently, in JJA, the combination of wetter soil and lower temperatures
382 facilitates vegetation photosynthesis in southern China, while drier soil largely contributes to
383 the reduction in GPP in the north and northeastern China (Figs. 5h, S5h, and S6h).

384



385 **3.3.3 National and regional total GPP anomalies**



386

387 Fig. 6. The seasonal and annual mean anomaly of GPP in different classified events for China (a), for
 388 Northern China (b), for Southern China (c), for Northwest China (d), and for Tibetan Plateau (e). The
 389 error bars show the standard deviation of different events in the composite analysis.

390

391 We calculated the total GPP anomaly in China and various geographic regions for each
 392 classified event on both seasonal and annual scales (Fig. 6). Regionally, the geographical
 393 divisions include Northern China, Southern China, Northwest China, and Tibetan Plateau (Fig.
 394 4e). Notably, the North-South boundary aligns closely with the 0° isotherm in January and the
 395 annual precipitation line of 800 mm. The division between the North and the Northwest is



396 determined by the annual precipitation line of 400 mm, and the Tibetan Plateau is segmented
397 based on topographic factors.

398

399 In general, the GPP anomalies exhibit noticeable differences on the seasonal scale, while the
400 total annual anomalies do not show a significant magnitude due to the mutual offset of positive
401 and negative anomalies in different seasons. However, it is worth noting that our annual totals
402 are calculated from the SON in the developing year of the event to the JJA in the following
403 year. This method deviates from the traditional calendar year, and as per the conventional
404 definition of a “year”, the annual anomalies induced by these events can indeed be substantial.

405

406 Specifically, taking a national perspective (Fig. 6a), GPP anomalies during the El Niño and La
407 Niña events exhibit opposite signs in DJF and JJA, with greater magnitudes during these peak
408 periods of the events and the most vigorous growth period of vegetation, respectively. In terms
409 of the development process of the event, the annual anomaly of GPP is negative during El Niño,
410 with a magnitude of -0.04 ± 0.19 Pg C yr⁻¹, but positive during La Niña events, with a
411 magnitude of 0.01 ± 0.37 Pg C yr⁻¹. The asymmetry of the positive and negative phases of IOD
412 is also evident in the total anomaly. For the pIOD event in 2019, GPP shows strong negative
413 anomalies with values of -0.41 Pg C yr⁻¹ in SON and -0.75 Pg C yr⁻¹ in DJF. Conversely, it
414 exhibits a marked positive anomaly in the following JJA, with a value of 0.85 Pg C yr⁻¹. The
415 annual total of GPP anomaly is opposite for pIOD and nIOD events, showing -0.10 Pg C yr⁻¹
416 and 0.01 ± 0.33 Pg C yr⁻¹, respectively. Moreover, large standard deviation indicated that there
417 are large uncertainties in the impact of different events, and each event has its uniqueness
418 (Capotondi et al., 2015).

419

420 Additionally, the variation of GPP anomaly in each region is basically consistent with that at
421 the national scale, especially in the Southern. But regional differences indeed exist in the total
422 amount of GPP anomalies, demonstrating the difference in the impact of events on different
423 regions’ GPP. Taking the 2019 extreme pIOD event as an example, the GPP showed a



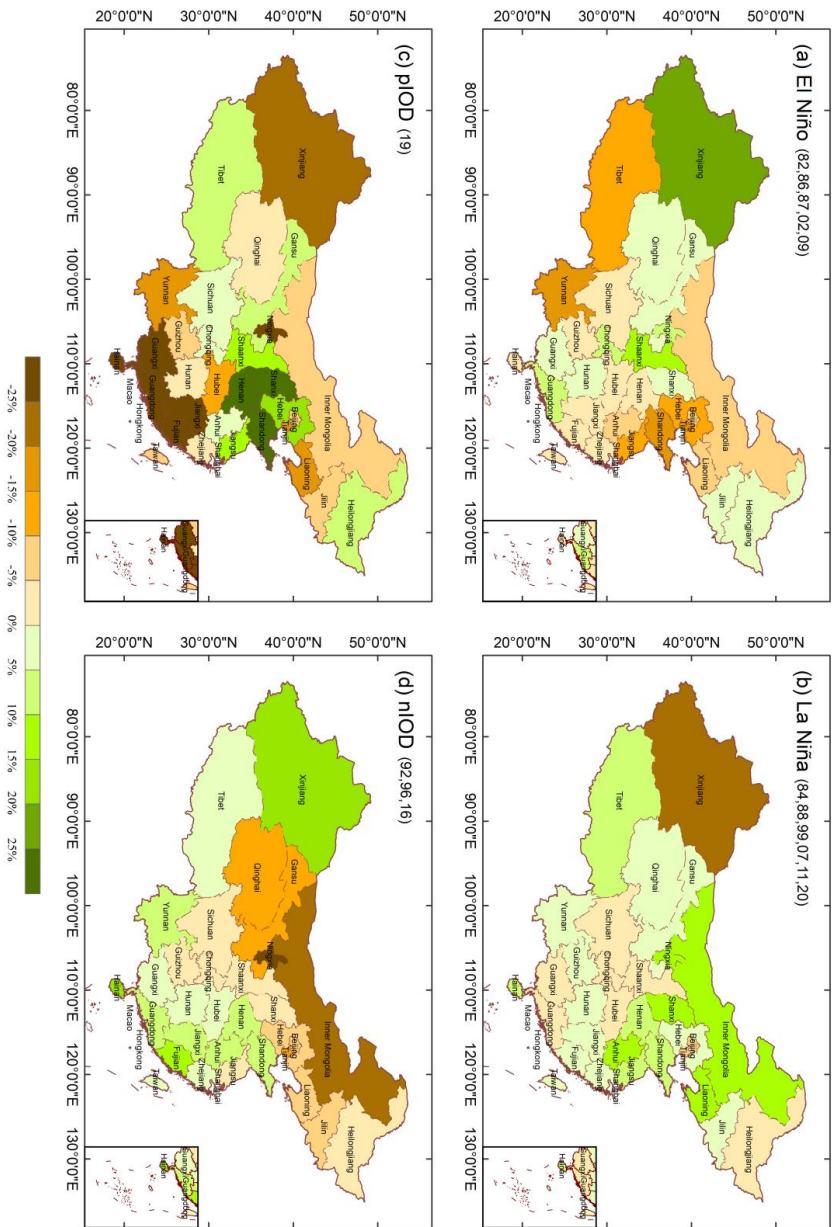
424 significant negative anomaly in the Southern during the SON (Fig. 6c), resulting in negative
425 anomalies in GPP at the national scale (Fig. 6a), but weak positive anomalies in the Northern
426 and TP (Figs. 6b and e). Then, the GPP anomaly was close to zero in the Northern and Southern
427 in MAM (Figs. 6b and c), while it was still a significant negative anomaly in the Northwest
428 and TP (Figs. 6d and e). Moreover, the negative annual GPP anomalies in the Southern and
429 Northwest offset the positive anomalies of the TP and Northern, making a negative annual GPP
430 anomaly in the national of this event.

431

432 In terms of the magnitude of GPP anomalies, they are more pronounced in the Northern and
433 Southern regions, characterized by lush vegetation, mostly less than 0.5 Pg C yr^{-1} .
434 Meanwhile, GPP anomalies are relatively weaker in the Northwest and TP regions, primarily
435 covered by grassland, generally less than 0.1 Pg C yr^{-1} . Further, we calculate the contributions
436 of different regions to the national total GPP anomaly in each event (Table S3), referencing an
437 index described in the article by Ahlstrom et al. (2015), as detailed in the supplementary method.
438 Overall, the GPP anomaly in the Southern region dominates the national GPP variation,
439 contributing approximately 68% to ENSO events and 46% to IOD events, respectively. The
440 Northern GPP anomaly contributes approximately 28% to the national GPP variation in ENSO
441 events and 39% in IOD events. In addition, the contribution of GPP anomaly in the Northwest
442 and TP regions to the national GPP variation is within 10%.



443 **3.3.4 Relative changes in total GDP anomalies at provincial scale**



444
 445 **Fig. 7. Spatial distributions of relative changes of total composite anomalies of GDP at provincial scale for different classified events.**



446 We presented the spatial patterns of mean GPP anomalies from the SON in the developing year
447 to the JJA in the decaying year (Fig. S7) and further calculated provincial total GPP anomalies
448 (Fig. S8 and Table S3). Provinces with more extensive forest coverage, such as Yunnan, central
449 provinces housing the Qinling Mountains, and northeast provinces where the Greater and
450 Lesser Hinggan Mountains are situated, exhibit relatively larger provincial GPP anomalies.
451 However, differences are apparent among different events (Fig. S8). Considering differences
452 in area and vegetation coverage across provinces, our focus centers on the relative change of
453 GPP anomalies (Fig. 7). It's important to note that, due to different years used in composite
454 analysis, our quantitative comparisons are limited to the same event within different provinces,
455 while qualitative descriptions are extended to different events.

456 El Niño events generally induce substantial GPP changes in two main regions with a relative
457 change of over 10% (Fig. 7a). One region encompasses the northern coastal provinces,
458 including Tianjin, Hebei, Shandong, and Jiangsu, while the other is situated in the western part,
459 including Xinjiang, Tibet, and Yunnan provinces. Yunnan, rich in forest resources, bears the
460 brunt of El Niño's impact, exhibiting a total negative GPP anomaly of $-90.21 \text{ Tg C yr}^{-1}$ (Table
461 S4) and a relative change of approximately 16%. Despite comparable relative changes in GPP
462 for other provinces, their GPP anomalies are relatively smaller, ranging from -10 to -15 Tg C
463 yr^{-1} . Notably, Xinjiang, characterized by a fragile forest steppe in the Altai and Tianshan
464 Mountain regions, consistently demonstrates substantial relative changes in GPP during both
465 ENSO and other events. Quantitatively, during the El Niño episode, Xinjiang witnesses a
466 remarkable 24% relative change in GPP, accompanied by a positive GPP anomaly of 15.27 Tg
467 C yr^{-1} . In contrast, during the La Niña episode, provinces with notable relative changes are
468 mainly concentrated in the northern regions, such as Xinjiang, Inner Mongolia, Ningxia,
469 Shanxi, and Liaoning provinces (Fig. 7b). In addition, although the influence of ENSO on GPP
470 in the southern China is significant (Fig. 4), the total relative change through the year remains
471 small due to the cancellation of positive and negative anomalies in different seasons.

472

473 In the pIOD classification, only the 2019 extreme event is considered, resulting in the relative



474 change in GPP anomalies exceeding 10% in approximately half of the provinces. Notably,
475 Jiangxi, Fujian, Guangxi, Guangdong, and Hainan experience reductions of more than 25% in
476 GPP, with Jiangxi exhibiting the largest GPP anomaly of $-130 \text{ Tg C yr}^{-1}$. Conversely,
477 Shandong, Shanxi, and Henan witness increase of over 25% in GPP (Fig. 7c). During nIOD
478 events, northern provinces generally exhibit negative relative changes, while southern
479 provinces display positive relative changes.

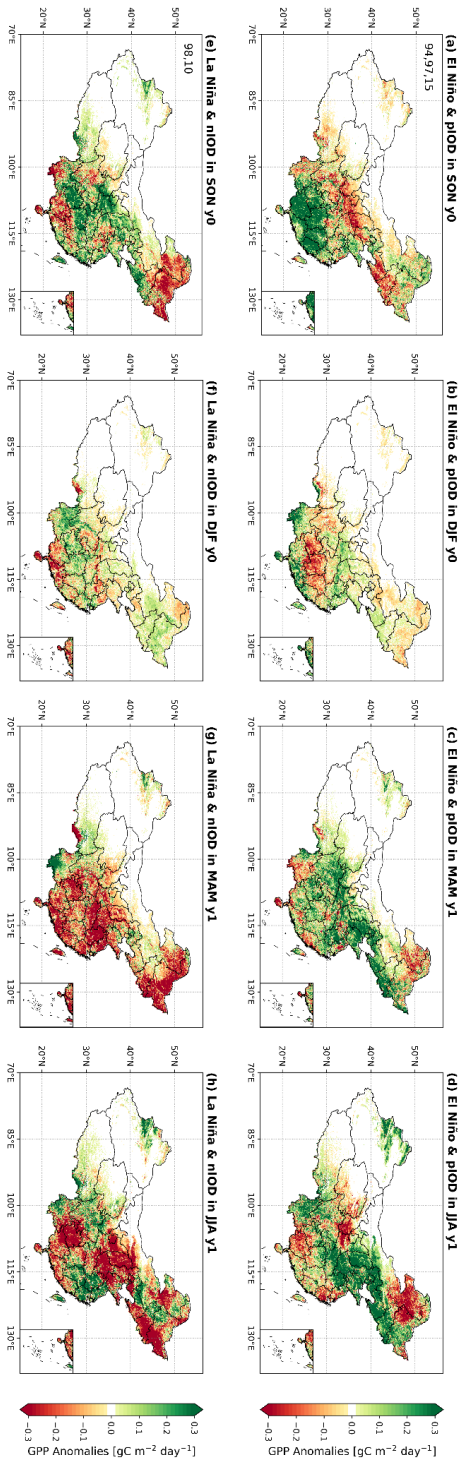
480

481 In summary, the relative changes in total GPP anomalies at the provincial scale exhibit an east-
482 west pattern in annual variation. Meanwhile, the influence of IOD events on GPP presents an
483 opposing north-south pattern.



484 **4. Discussion**

485 **4.1 The effect of compound ENSO and IOD events on China's GPP**



486
 487 **Fig. 8.** Spatial distributions of seasonal composite GPP anomalies for compound events, (a-d) for El Niño & pIOD events, and (e-h) for La Niña & nIOD events.
 488 The two-digit year in first column denote the years used for composite analysis.



489 Indeed, despite IOD events being generally considered an independent coupled ocean-
490 atmosphere interaction (Saji et al., 1999), historical IOD events can occur in conjunction with
491 ENSO (Ham et al., 2017; Yang et al., 2015). These combined phenomena are most notable
492 represented by El Niño & pIOD and La Niña & nIOD events. Williams and Hanan (2011)
493 researched the interactive effects of ENSO and IOD on African GPP, relying on an offline
494 terrestrial biosphere model simulation. Their findings suggested that IOD could cause obvious
495 anomalous GPP over much of Africa, capable of suppressing or even reversing ENSO signals
496 in GPP anomalies. In addition, Yan et al. (2023) explored the interactive effects of ENSO and
497 IOD on seasonal anomalies of tropical net land carbon flux using the TRENDYv9 multi-model
498 simulations, revealing diverse effects in different sub-continent and seasons. We explore the
499 anomalies of GPP in compound events based on composite analysis (Fig. 8), and the spatial
500 patterns of soil moisture and temperature anomalies are shown in the appendix (Figs. S9 and
501 S10).

502

503 The spatial patterns of the GPP anomalies during concurrent ENSO and IOD events differ from
504 those in single events, although some similarities are evident. GPP anomalies in El Niño &
505 pIOD and La Niña & nIOD events are generally opposite, and we focus specifically on El Niño
506 & pIOD events here. In El Niño & pIOD events, GPP anomalies exhibit a general opposition,
507 with enhanced vegetation photosynthesis in the southern regions and inhibited in the northern
508 regions during SON. This spatial characteristic of GPP anomalies bears some resemblance to
509 that induced by El Niño alone (Figs. 4a and 8a). Weak GPP anomalies are generally observed
510 in DJF, with noticeable negative GPP anomalies in Guizhou and Hunan, and some positive
511 GPP anomalies in regions south of 25°N (Fig. 8b). Notably during DJF, while significant
512 positive GPP anomalies occur in El Niño events (Fig. 4b), simultaneous pIOD events induce
513 significant negative GPP anomalies (Fig. 5b). When both events coincide, their impacts seem
514 to largely counterbalance each other, resulting in a more neutral GPP anomaly. In MAM, GPP
515 increases in Northern China (Fig. 8c). Subsequently, in JJA, vegetation photosynthesis
516 experiences a significant increase in the Northern and Yunnan provinces (Fig. 8d).



517 It is worth noting that the impacts of compound events on China's GPP may not follow a
518 straightforward linear superposition of the effects of two individual events. While their effects
519 are nearly opposite when occurring separately, the positive and negative effects on GPP may
520 be not simply cancelled each other out when they coincide. This complexity arises from the
521 simultaneous occurrence of two tropical air-sea interaction modes, leading to intricate effects
522 on mid-latitude circulations. Given the limited number of compound events, further exploration
523 is necessary to unravel the effects of ENSO and IOD on GPP in China.

524

525 **4.2 Modulation of large-scale circulations on China's GPP**

526 China's GPP is intricately influenced by atmospheric circulations and sea surface temperature
527 (Li et al., 2021; Ying et al., 2022). Ying et al. (2022) showed significant correlations between
528 seasonal GPP variation in China and climate phenomena such as ENSO, Pacific Decadal
529 Oscillation (PDO), and Arctic Oscillation (AO), based on the Residual Principal Component
530 analysis. Their research indicated that these identified SST and circulation factors could
531 account for 13%, 23% and 19% of the seasonal GPP variations in spring, summer and autumn,
532 respectively. And Li et al. (2021) proved that GPP response to El Niño varied with PDO phases
533 during the growing seasons of typical El Niño years. Although both studies emphasized the
534 impact of ENSO on China's GPP and explored the roles of PDO and AO, the IOD was notably
535 absent from their analyses. Contrastingly, our study sheds light on the significant influence of
536 the extreme positive phase of IOD in 2019, showing a substantial negative GPP anomaly in
537 southeastern China during SON, aligning with findings by Wang et al. (2021b). Moreover, the
538 integration of partial correlation and composite analysis in our study elucidates the
539 considerable impact of IOD on China's GPP within this context. Importantly, our research
540 underscores the temporal and spatial variability in the effects of IOD and ENSO on GPP across
541 different seasons and regions. This complexity in ocean-atmosphere teleconnections implies
542 that other climate oscillations, such as Polar/Eurasia (polarEA) and Atlantic Multidecadal
543 Oscillation (AMO), might also contribute to influencing China's GPP (Zhu et al., 2017), which



544 is still worthy of further analysis and research.

545

546 **4.3 Uncertainties in BEPS Simulations**

547 The simulation of China's GPP by BEPS is subject to several sources of uncertainty inherent
548 in the model's structure, parameterizations, processes, and input data (Chen et al., 2012; Chen
549 et al., 2017; He et al., 2021a; Liu et al., 2018; Wang et al., 2021a). Leaf Area Index (LAI), a
550 crucial input for the BEPS model, is derived from global remote sensing data that inherently
551 possess uncertainties in spatial distribution and trend changes. Previous studies have
552 highlighted significant uncertainties in simulating carbon budget of global terrestrial
553 ecosystems when employing different LAI remote sensing data (Chen et al., 2019; Liu et al.,
554 2018). Foliage clumping index which is used to separate sunlit and shaded LAI can also cause
555 some uncertainties in simulating GPP, because the current version of BEPS used the time-
556 invariant satellite-derived clumping index (Chen et al., 2012). Biases in meteorological drivers,
557 such as precipitation, can further result in considerable uncertainties in simulating terrestrial
558 carbon cycle. The choice of precipitation products, for instance, has been shown to yield
559 considerable differences in simulated net land-atmosphere carbon flux (Wang et al., 2021c).
560 Moreover, BEPS model, like other terrestrial biosphere models, lacks consideration for
561 vegetation adaptability to rising CO₂ concentration, potentially leading to an overestimation of
562 the fertilization effect on GPP. In addition, the accuracy of simulations over agricultural areas
563 is compromised in BEPS, as it only considers crops with a C3 photosynthetic pathway and
564 overlooks C4 crops (He et al., 2017; He et al., 2021b; Ju et al., 2006). Although BEPS simulated
565 GPP demonstrates relatively high consistency with the measured GPP of Yingke Station (CRO),
566 located in the northwest of China, its accuracy lacks validation over the extensive farmlands in
567 north and northeastern China where various crops are grown (Fig. S11). Agricultural operations,
568 particularly irrigation, which can significantly impact GPP, are not considered in BEPS. He et
569 al. (2021a) revealed extensive wetting signals over croplands in arid and semi-arid areas which
570 exerted strong impacts on GPP and evapotranspiration simulations in BEPS after assimilating



571 the Soil Moisture Active Passive (SMAP) soil moisture product. Furthermore, photosynthetic
572 key parameters, such as carboxylation capacity at 25°C ($V_{\text{cmax},25}$), can largely determine the
573 performance in simulating GPP. After assimilating the solar-induced chlorophyll fluorescence
574 (SIF) from the Orbiting Carbon Observing Satellite-2 (OCO-2) to optimize $V_{\text{cmax},25}$ of different
575 plant functional types (PFTs) in BEPS, previous studies suggested the improvements in
576 simulating GPP at regional and global scales to some extent (He et al., 2019; Wang et al.,
577 2021a).

578

579 **5. Conclusion**

580 In this paper, we used partial correlation coefficients and composite analysis to investigate the
581 impacts of ENSO and IOD events on China's GPP during 1981–2021. The partial correlation
582 results reveal that the effects of ENSO and IOD on GPP and related climate in China exhibit
583 distinct seasonal variations and are basically opposite. Specifically, during SON, significant
584 negative *pcor* between GPP and ENSO is observed over the Tibetan Plateau, southwestern
585 China, Loess Plateau, and Liaoning. In DJF, strongly positive *pcor* occurs over southern China,
586 weakening in the subsequent MAM, albeit with some enhancements in northern Hebei and
587 neighboring Inner Mongolia. The *pcor* then turns generally negative in JJA. In contrast,
588 significant positive *pcor* between GPP and IOD is noted in southwestern and Northeast China
589 during SON. Subsequently, widespread negative *pcor* appears during DJF, persisting
590 significantly in most western and northern regions during MAM. In JJA, the *pcor* becomes
591 significantly positive in southwestern, north and northeast China. Moreover, the correlation
592 coefficients between GPP and climate show that GPP anomalies are primarily dominated by
593 SM in JJA and SON, while temperature generally plays a more important role in in DJF and
594 MAM.

595

596 The composite analysis results validate the patterns of GPP anomalies observed in the partial
597 correlation. Generally, China's annual total GPP demonstrates modest positive anomalies in La



598 Niña and nIOD years, contrasting with minor negative anomalies in El Niño and pIOD years.
599 This results from the counterbalancing effects, with significantly greater GPP anomalous
600 magnitudes in DJF and JJA. Regionally, GPP anomalies fluctuate more in the Southern and
601 Northern regions. The GPP anomaly in the Southern region dominates the national GPP
602 variation, with the contribution of 68% to ENSO events and 46% to IOD events, respectively.
603 On the provincial scale, western and northern provinces in experience larger relative annual
604 variations during ENSO events, with magnitudes exceeding 10%, exhibiting a general east-
605 west pattern. Conversely, provinces in the southern and Northern China witness larger relative
606 changes during IOD events, showing an opposing north-south pattern. For instance, the 2019
607 extreme pIOD led to relative changes of over 25% in certain provinces in the south and north.
608



609 **Acknowledgement**

610 The calculations in this paper have been done on the computing facilities in the High Performance
611 Computing Center (HPCC) of Nanjing University. This study was supported by the Natural Science
612 Foundation of China (Grants 42141005), the Natural Science Foundation of Jiangsu Province, China
613 (BK20221449), and the National Key Scientific and Technological Infrastructure project “Earth System
614 Numerical Simulation Facility” (grant 2023-EL-ZD-00022).

615

616 **Conflict of Interest**

617 The authors declare no competing interests.

618

619 **Data Availability**

620 REA5 meteorological data are available at <https://cds.climate.copernicus.eu/cdsapp#!/dataset/reanalysis-era5-single-levels?tab=overview>. The remote-sensing GLOBMAP LAI data is available at
621 <https://zenodo.org/record/4700264#.YzvSYnZBxD8/>. The carbon dioxide emissions data is available at
622 https://gml.noaa.gov/webdata/ccgg/trends/co2/co2_mm_mlo.txt. Vegetation type data for B
623 EPS simulations is obtained from <https://lpdaac.usgs.gov/products/mcd12q1v006/>. Soil texture data is available at <https://data.tpdc.ac.cn/zh-hans/data/611f7d50-b419-4d14-b4dd-4a944b141175>. Soil
624 moisture and surface air temperature from ERA5-Land are available at <https://cds.climate.copernicus.eu/cdsapp#!/dataset/reanalysis-era5-land-monthly-means?tab=overview>. Sea surface temperature dataset from ERSSTv5 is available at <https://psl.noaa.gov/data/gridded/data.noaa.ersst.v5.html>. Eight sites of the ten are from ChinaFlux (<http://www.chinaflux.org/enn/index.aspx>), and
629 two are from National Tibetan Plateau Third Pole Environment (<http://data.tpdc.ac.cn/zh-hans>).
630 FluxSat GPP Version 2.2 are available at https://avdc.gsfc.nasa.gov/pub/tmp/FluxSat_GPP.

632



633 **Reference**

- 634 Ahlstrom, A., et al., 2015: The dominant role of semi-arid ecosystems in the trend and variability of the
635 land CO₂ sink, *SCIENCE*, 348(6237), 895-899, [https://doi:10.1126/science.aaa1668](https://doi.org/10.1126/science.aaa1668).
- 636 Bauch, M., 2020: Chapter 15 - Impacts of extreme events on medieval societies: Insights from climate
637 history, in *Climate Extremes and Their Implications for Impact and Risk Assessment*, edited by J.
638 Sillmann, S. Sippel and S. Russo, pp. 279-291, Elsevier, [https://doi.org/10.1016/B978-0-12-814895-](https://doi.org/10.1016/B978-0-12-814895-2.00015-X)
639 [2.00015-X](https://doi.org/10.1016/B978-0-12-814895-2.00015-X).
- 640 Capotondi, A., et al., 2015: Understanding ENSO Diversity, *B. AM. METEOROL. SOC.*, 96(6), 921-
641 938, [https://doi:10.1175/BAMS-D-13-00117.1](https://doi.org/10.1175/BAMS-D-13-00117.1).
- 642 Chen, J. M., W. Ju, P. Ciais, N. Viovy, R. Liu, Y. Liu, and X. Lu, 2019: Vegetation structural change
643 since 1981 significantly enhanced the terrestrial carbon sink, *NAT. COMMUN.*, 10,
644 [https://doi:10.1038/s41467-019-12257-8](https://doi.org/10.1038/s41467-019-12257-8).
- 645 Chen, J. M., J. Liu, J. Cihlar, and M. L. Goulden, 1999: Daily canopy photosynthesis model through
646 temporal and spatial scaling for remote sensing applications, *ECOL. MODEL.*, 124(2-3), 99-119,
647 [https://doi:10.1016/S0304-3800\(99\)00156-8](https://doi.org/10.1016/S0304-3800(99)00156-8).
- 648 Chen, J. M., G. Mo, J. Pisek, J. Liu, F. Deng, M. Ishizawa, and D. Chan, 2012: Effects of foliage
649 clumping on the estimation of global terrestrial gross primary productivity, *GLOBAL BIOGEOCHEM.*
650 *CY.*, 26(1), GB1019, [https://doi:10.1029/2010gb003996](https://doi.org/10.1029/2010gb003996).
- 651 Chen, Z., J. M. Chen, S. Zhang, X. Zheng, W. Ju, G. Mo, and X. Lu, 2017: Optimization of Terrestrial
652 Ecosystem Model Parameters Using Atmospheric CO₂ Concentration Data With the Global Carbon
653 Assimilation System (GCAS), *J. GEOPHYS. RES. - BIOGEO.*, 122, 3218-3237,
654 <http://doi.org/10.1002/2016JG003716>.
- 655 Chen, J.M. et al., 2019. Vegetation structural change since 1981 significantly enhanced the terrestrial
656 carbon sink. *Nature Communications*, 10(1): 4259.
- 657 Gough, C. (2012): Terrestrial primary production: Fuel for life, *Nature Education Knowledge*, 3.
- 658 Ham, Y.-G., J.-Y. Choi, and J.-S. Kug, 2017: The weakening of the ENSO–Indian Ocean Dipole (IOD)
659 coupling strength in recent decades, *CLIM. DYNAM.*, 49(1), 249-261, [https://doi:10.1007/s00382-016-](https://doi.org/10.1007/s00382-016-3339-5)
660 [3339-5](https://doi.org/10.1007/s00382-016-3339-5).



- 661 He, B., et al., 2022: Worldwide impacts of atmospheric vapor pressure deficit on the interannual
662 variability of terrestrial carbon sinks, *NATL. SCI. REV.*, 9(4), nwab150,
663 <https://doi:10.1093/nsr/nwab150>.
- 664 He, L., J. M. Chen, J. Liu, S. Bélair, and X. Luo, 2017: Assessment of SMAP soil moisture for global
665 simulation of gross primary production, *J. GEOPHYS. RES. - BIOGEO.*, 122(7), 1549-1563,
666 <https://doi:10.1002/2016jg003603>.
- 667 He, L., J. M. Chen, G. Mostovoy, and A. Gonsamo, 2021a: Soil Moisture Active Passive Improves
668 Global Soil Moisture Simulation in a Land Surface Scheme and Reveals Strong Irrigation Signals Over
669 Farmlands, *Geophys. Res. Lett.*, 48(8), <https://doi:10.1029/2021gl092658>.
- 670 He, L., R. Wang, G. Mostovoy, J. Liu, J. M. Chen, J. Shang, J. Liu, H. McNairn, and J. Powers, 2021b:
671 Crop Biomass Mapping Based on Ecosystem Modeling at Regional Scale Using High Resolution
672 Sentinel-2 Data, *REMOTE SENS.*, 13(4), <https://doi:10.3390/rs13040806>.
- 673 He, L. M., et al., 2019: Diverse photosynthetic capacity of global ecosystems mapped by satellite
674 chlorophyll fluorescence measurements, *REMOTE SENS. ENVIRON.*, 232,
675 <https://doi:10.1016/j.rse.2019.111344>.
- 676 He, Q. et al., 2021. Drought Risk of Global Terrestrial Gross Primary Productivity Over the Last 40
677 Years Detected by a Remote Sensing-Driven Process Model. *Journal of Geophysical Research:*
678 *Biogeosciences*, 126(6): e2020JG005944.
- 679 Hersbach, H., Bell, B., Berrisford, P., Biavati, G., Horányi, A., Muñoz Sabater, J., Nicolas, J., Peubey,
680 C., Radu, R., Rozum, I., Schepers, D., Simmons, A., Soci, C., Dee, D., Thépaut, J-N. (2023): ERA5
681 hourly data on single levels from 1940 to present. Copernicus Climate Change Service (C3S) Climate
682 Data Store (CDS), DOI: 10.24381/cds.adbb2d47.
- 683 Houghton, R. A., 2007: Balancing the global carbon budget, *ANNU. REV. EARTH. PL. SC.*, 35, 313-
684 347, <https://doi:10.1146/annurev.earth.35.031306.140057>.
- 685 Joiner, J., Y. Yoshida, Y. Zhang, G. Duveiller, M. Jung, A. Lyapustin, Y. Wang, and C. J. Tucker (2018):
686 Estimation of Terrestrial Global Gross Primary Production (GPP) with Satellite Data-Driven Models
687 and Eddy Covariance Flux Data, *REMOTE SENS.*, 10(9), <https://doi:10.3390/rs10091346>.
- 688 Ju, W., J. M. Chen, T. A. Black, A. G. Barr, J. Liu, and B. Chen, 2006: Modelling multi-year coupled



- 689 carbon and water fluxes in a boreal aspen forest, *AGR. FOREST METEOROL.*, 140(1-4), 136-151,
690 <https://doi:10.1016/j.agrformet.2006.08.008>.
- 691 Fischer, G., F. Nachtergaele, S. Prieler, H.T. van Velthuisen, L. Verelst, D. Wiberg, 2008. Global Agro-
692 ecological Zones Assessment for Agriculture (GAEZ 2008). IIASA, Laxenburg, Austria and FAO,
693 Rome, Italy.
- 694 Friedl, M., Sulla-Menashe, D., 2019. *MCD12Q1 MODIS/Terra+Aqua Land Cover Type Yearly L3*
695 *Global 500m SIN Grid V006* [Data set]. NASA EOSDIS Land Processes Distributed Active Archive
696 Center.
- 697 Kim, J. S., J. S. Kug, and S. J. Jeong, 2017: Intensification of terrestrial carbon cycle related to El Nino-
698 Southern Oscillation under greenhouse warming, *NAT. COMMUN.*, 8, [https://doi:10.1038/s41467-017-](https://doi:10.1038/s41467-017-01831-7)
699 [01831-7](https://doi:10.1038/s41467-017-01831-7).
- 700 Lan, X., Tans, P. and K.W. Thoning: Trends in globally-averaged CO₂ determined from NOAA Global
701 Monitoring Laboratory measurements. Version 2024-04 <https://doi.org/10.15138/9N0H-ZH07>.
- 702 Li, X., et al., 2013. Heihe watershed allied telemetry experimental research (HiWATER): scientific
703 objectives and experimental design. *Bull. Am. Meteorol. Soc.* 94 (8), 1145–1160.
- 704 Li, Y., L. Dan, J. Peng, J. Wang, F. Yang, D. Gao, X. Yang, and Q. Yu, 2021: Response of Growing
705 Season Gross Primary Production to El Niño in Different Phases of the Pacific Decadal Oscillation over
706 Eastern China Based on Bayesian Model Averaging, *ADV. ATMOS. SCI.*, 38(9), 1580-1595,
707 <https://doi:10.1007/s00376-021-0265-1>.
- 708 Liu, J., J. M. Chen, J. Cihlar, and W. M. Park, 1997: A process-based boreal ecosystem productivity
709 simulator using remote sensing inputs, *REMOTE SENS. ENVIRON.*, 62(2), 158-175,
710 [https://doi.org/10.1016/S0034-4257\(97\)00089-8](https://doi.org/10.1016/S0034-4257(97)00089-8).
- 711 Liu, Y., Liu, R., Chen, J.M., 2012. Retrospective retrieval of long-term consistent global leaf area index
712 (1981-2011) from combined AVHRR and MODIS data. *J. Geophys. Res. Biogeosci.* 117 (G4), G04003.
- 713 Liu, Y., J. Xiao, W. Ju, G. Zhu, X. Wu, W. Fan, D. Li, and Y. Zhou, 2018: Satellite-derived LAI products
714 exhibit large discrepancies and can lead to substantial uncertainty in simulated carbon and water fluxes,
715 *REMOTE SENS. ENVIRON.*, 206, 174-188, <https://doi:10.1016/j.rse.2017.12.024>.
- 716 Liu, Y., X. Yang, E. Wang, and C. Xue, 2014: Climate and crop yields impacted by ENSO episodes on



- 717 the North China Plain: 1956-2006, *REG. ENVIRON. CHANGE.*, 14(1), 49-59,
718 [https://doi:10.1007/s10113-013-0455-1](https://doi.org/10.1007/s10113-013-0455-1).
- 719 Mercado, L. M., N. Bellouin, S. Sitch, O. Boucher, C. Huntingford, M. Wild, and P. M. Cox, 2009:
720 Impact of changes in diffuse radiation on the global land carbon sink, *NATURE*, 458(7241), 1014-1017,
721 [https://doi:10.1038/nature07949](https://doi.org/10.1038/nature07949).
- 722 Muñoz, S. J., 2019: ERA5-Land monthly averaged data from 1950 to present. *Copernicus Climate*
723 *Change Service (C3S) Climate Data Store (CDS)*.
- 724 Norman, J. M., 1982: Simulation of microclimates. In: Hatfield, J.L., Thomason, I.J. (Eds.),
725 *Biometeorology in Integrated Pest Management* (pp. 65–99). New York, CA: Academic Press.
- 726 Piao, S., X. Wang, K. Wang, X. Li, A. Bastos, J. G. Canadell, P. Ciais, P. Friedlingstein, and S. Sitch
727 2020: Interannual variation of terrestrial carbon cycle: Issues and perspectives, *GLOBAL CHANGE*
728 *BIOL.*, 26(1), 300-318, [https://doi:10.1111/gcb.14884](https://doi.org/10.1111/gcb.14884).
- 729 Ryu, Y., J. A. Berry, and D. D. Baldocchi, 2019: What is global photosynthesis? History, uncertainties
730 and opportunities, *REMOTE SENS. ENVIRON.*, 223, 95-114, [https://doi:10.1016/j.rse.2019.01.016](https://doi.org/10.1016/j.rse.2019.01.016).
- 731 Saji, N. H., B. N. Goswami, P. N. Vinayachandran, and T. Yamagata (1999: A dipole mode in the tropical
732 Indian Ocean, *NATURE*, 401(6751), 360-363, [https://doi:10.1038/43855](https://doi.org/10.1038/43855).
- 733 Saji, N. H., and T. Yamagata, 2003: Possible impacts of Indian Ocean Dipole mode events on global
734 climate, *CLIM. RES.*, 25(2), 151-169, [https://doi:10.3354/cr025151](https://doi.org/10.3354/cr025151).
- 735 Schimel, D., B. B. Stephens, and J. B. Fisher, 2015: Effect of increasing CO₂ on the terrestrial carbon
736 cycle, *P. NATL. ACAD. SCI. USA.*, 112(2), 436-441, [https://doi:10.1073/pnas.1407302112/-](https://doi.org/10.1073/pnas.1407302112/-/DCSupplemental)
737 */DCSupplemental*.
- 738 Wang, J., et al., 2022: Enhanced India-Africa Carbon Uptake and Asia-Pacific Carbon Release
739 Associated With the 2019 Extreme Positive Indian Ocean Dipole, *Geophys. Res. Lett.*, 49(22),
740 [https://doi:10.1029/2022gl100950](https://doi.org/10.1029/2022gl100950).
- 741 Wang, J., F. Jiang, H. Wang, B. Qiu, M. Wu, W. He, W. Ju, Y. Zhang, J. M. Chen, and Y. Zhou, 2021a:
742 Constraining global terrestrial gross primary productivity in a global carbon assimilation system with
743 OCO-2 chlorophyll fluorescence data, *AGR. FOREST METEOROL.*, 304-305,
744 [https://doi:10.1016/j.agrformet.2021.108424](https://doi.org/10.1016/j.agrformet.2021.108424).



- 745 Wang, J., Z. Liu, N. Zeng, F. Jiang, H. Wang, and W. Ju, 2020: Spaceborne detection of XCO₂
746 enhancement induced by Australian mega-bushfires, *ENVIRON. RES. LETT.*, 15(12),
747 <https://doi:10.1088/1748-9326/abc846>.
- 748 Wang, J., et al., 2021b: Modulation of Land Photosynthesis by the Indian Ocean Dipole: Satellite-Based
749 Observations and CMIP6 Future Projections, *Earth's Future*, 9(4), <https://doi:10.1029/2020ef001942>.
- 750 Wang, J., et al., 2023: Anomalous Net Biome Exchange Over Amazonian Rainforests Induced by the
751 2015/16 El Niño: Soil Dryness-Shaped Spatial Pattern but Temperature-dominated Total Flux, *Geophys.*
752 *Res. Lett.*, 50(11), <https://doi:10.1029/2023GL103379>.
- 753 Wang, J., N. Zeng, and M. Wang, 2016: Interannual variability of the atmospheric CO₂ growth rate:
754 roles of precipitation and temperature, *BIOGEOSCIENCES*, 13(8), 2339-2352, [https://doi:10.5194/bg-](https://doi:10.5194/bg-13-2339-2016)
755 13-2339-2016.
- 756 Wang, J., et al., 2018: Contrasting interannual atmospheric CO₂ variabilities and their terrestrial
757 mechanisms for two types of El Niños, *ATMOS. CHEM. PHYS.*, 18(14), 10333-10345,
758 <https://doi:10.5194/acp-18-10333-2018>.
- 759 Wang, M., J. Wang, Q. Cai, N. Zeng, X. Lu, R. Yang, F. Jiang, H. Wang, and W. Ju, 2021c: Considerable
760 Uncertainties in Simulating Land Carbon Sinks Induced by Different Precipitation Products, *J.*
761 *GEOPHYS. RES. - BIOGEO.*, 126(10), e2021JG006524, <https://doi.org/10.1029/2021JG006524>.
- 762 Williams, C. A., and N. P. Hanan, 2011: ENSO and IOD teleconnections for African ecosystems:
763 evidence of destructive interference between climate oscillations, *BIOGEOSCIENCES*, 8(1), 27-40,
764 <https://doi:10.5194/bg-8-27-2011>.
- 765 Yan, R., J. Wang, W. Ju, D. S. Goll, A. K. Jain, S. Sitch, H. Tian, P. Benjamin, F. Jiang, and H. Wang,
766 2023: Interactive effects of the El Niño-Southern Oscillation and Indian Ocean Dipole on the tropical
767 net ecosystem productivity, *AGR. FOREST METEOROL.*, 336, 109472,
768 <https://doi.org/10.1016/j.agrformet.2023.109472>.
- 769 Yang, R., et al., 2022: Divergent historical GPP trends among state-of-the-art multi-model simulations
770 and satellite-based products, *EARTH SYST. DYNAM.*, 13(2), 833-849, [https://doi:10.5194/esd-13-833-](https://doi:10.5194/esd-13-833-2022)
771 2022.
- 772 Yang, Y., S.-P. Xie, L. Wu, Y. Kosaka, N.-C. Lau, and G. A. Vecchi, 2015: Seasonality and Predictability



773 of the Indian Ocean Dipole Mode: ENSO Forcing and Internal Variability, *J. CLIMATE*, 28(20), 8021-
774 8036, [https://doi:10.1175/JCLI-D-15-0078.1](https://doi.org/10.1175/JCLI-D-15-0078.1).

775 Ying, K., J. Peng, L. Dan, and X. Zheng, 2022: Ocean—atmosphere Teleconnections Play a Key Role
776 in the Interannual Variability of Seasonal Gross Primary Production in China, *ADV. ATMOS. SCI.*, 39(8),
777 1329-1342, [https://doi:10.1007/s00376-021-1226-4](https://doi.org/10.1007/s00376-021-1226-4).

778 Zeng, N., A. Mariotti, and P. Wetzzel, 2005: Terrestrial mechanisms of interannual CO₂ variability,
779 *GLOBAL BIOGEOCHEM. CY.*, 19(1), [https://doi:10.1029/2004gb002273](https://doi.org/10.1029/2004gb002273).

780 Zhang, X., Y. P. Wang, S. Peng, P. J. Rayner, P. Ciais, J. D. Silver, S. Piao, Z. Zhu, X. Lu, and X. Zheng,
781 2018: Dominant regions and drivers of the variability of the global land carbon sink across timescales,
782 *GLOBAL CHANGE BIOL.*, 24(9), 3954-3968, [https://doi:10.1111/gcb.14275](https://doi.org/10.1111/gcb.14275).

783 Zhang, Y., M. P. Dannenberg, T. Hwang, and C. Song, 2019: El Niño-Southern Oscillation-Induced
784 Variability of Terrestrial Gross Primary Production During the Satellite Era, *J. GEOPHYS. RES. -*
785 *BIOGEO.*, 124(8), 2419-2431, [https://doi:10.1029/2019jg005117](https://doi.org/10.1029/2019jg005117).

786 Zhang, Y., W. Zhou, X. Wang, X. Wang, R. Zhang, Y. Li, and J. Gan, 2022a: IOD, ENSO, and seasonal
787 precipitation variation over Eastern China, *ATMOS. RES.*, 270,
788 [https://doi:10.1016/j.atmosres.2022.106042](https://doi.org/10.1016/j.atmosres.2022.106042).

789 Zhang, Y., W. Zhou, X. Wang, S. Chen, J. Chen, and S. Li, 2022b: Indian Ocean Dipole and ENSO's
790 mechanistic importance in modulating the ensuing-summer precipitation over Eastern China, *NPJ*
791 *CLIM. ATMOS. SCI.*, 5(1), [https://doi:10.1038/s41612-022-00271-5](https://doi.org/10.1038/s41612-022-00271-5).

792 Zhu, Z., S. Piao, Y. Xu, A. Bastos, P. Ciais, and S. Peng, 2017: The effects of teleconnections on carbon
793 fluxes of global terrestrial ecosystems, *Geophys. Res. Lett.*, 44(7), 3209-3218,
794 [https://doi:10.1002/2016GL071743](https://doi.org/10.1002/2016GL071743).